

This is a non-peer reviewed pre-print submitted to EarthArXiv.

Subsequent peer-reviewed versions of this manuscript may have slightly different content.

The author welcome feedback.

Please contact Sandy H.S. Herho (herho@umd.edu) regarding this manuscript's content.

Long-term hydrometeorological time-series analysis over the central highlands of West Papua

Sandy H.S. Herho

Department of Geology,
College of Computer, Mathematical, and Natural Sciences,
University of Maryland,
College Park, MD, USA 20742
herho@umd.edu

Abstract

1 This article presents a novel data-driven approach for studying long-term tem-
2 poral rainfall pattern over the central highlands of West Papua, Indonesia. Us-
3 ing wavelet transforms we found indications of negative temporal relationship of
4 El Niño - Southern Oscillation (ENSO) and 12-month Standardized Precipitation
5 Index (SPI-12). Based on this causal relationship, we perform dynamic causal-
6 ity modeling using the Nonlinear Autoregressive with Exogenous input (NARX)
7 model to predict SPI-12 using the Multivariate ENSO Index (MEI) as an attribute
8 variable. As a result, this dynamic neural network model is able to capture com-
9 mon features in the SPI-12 time series. This study has a profound impact for the
10 future development of data-driven precipitation models for areas with complex
11 topography in Indonesian Maritime Continent (IMC).

12 *key words: ENSO, NARX, SPI, wavelet transform*

13 1 Introduction

14 The central highlands of West Papua is part of the province of Papua, which is the easternmost
15 province of Indonesia (Figure 1). This region has a complex landscape with rugged and hilly terrain.
16 Some of the highest peaks in Indonesia, such as Carstensz Pyramid (5030 m.a.s.l), Trikora Peak
17 (4730 masl), Yamin Peak (4595 m.a.s.l), and Mandala Peak (4700 m.a.s.l) are also located in the
18 central highlands of West Papua. This complex geomorphological appearance is an expression of
19 the geological and tectonic conditions that have occurred in that place. According to (author?) (1)
20 the island of Papua was formed from a process of subduction between the Australian Plate and the
21 Pacific Plate. The convergent process and deformation of these two plates began in the Eocene and
22 continues to the present (2). The Australian Plate, which is under the Arafura Sea and extends to the
23 north, is the base of the southern part of the central highlands of West Papua, where the base layer
24 is composed of sedimentary rocks within the ages ranging from Paleozoic to Mid-Quaternary (3).

25 The central highlands of West Papua stretches from the equator to 12°S. This area can be classified
26 as a tropical region dominated seasonally by the monsoonal asymmetric cycle, like most areas in
27 the Indonesian Maritime Continent (IMC) (4; 5). Apart from monsoonal influences, as in other
28 areas in the IMC, central highlands of West Papua there are also local influences, such as mountain
29 deflection and local warming which control rainfall circulation in this area (6). In addition, El Niño
30 - Southern Oscillation (ENSO) also has an impact on seasonal rainfall conditions in Papua, El Niño
31 events can reduce rainfall in the area (7). This region experiences variations in precipitation between
32 2500 – 4500 mm/year with the number of rainy days varying from 148 to 175 rainy days/year with
33 average surface air temperatures of 29°C to 31.8°C and relative humidity varying between 79% to
34 81%. Thus, the central highlands of Papua is one of the wettest areas in the IMC (8).

35 Studies that discuss the characteristics of rainfall in the Papua region are still difficult to find. This
 36 can be due to the complex regional topography in this area which makes it difficult to study it using
 37 a numerical approaches (9). Besides, this can also be caused by aerial coverage of rain gauges
 38 and radar networks owned by the Indonesian Agency for Meteorology Climatology and Geophysics
 39 (BMKG) (10). To solve this problem, we offer a solution by using a data-driven approach (11)
 40 by utilizing ERA5 monthly averaged data on single levels (12) to reveal the characteristics and
 41 predictability of long-term precipitation time series over the central highlands of Papua.

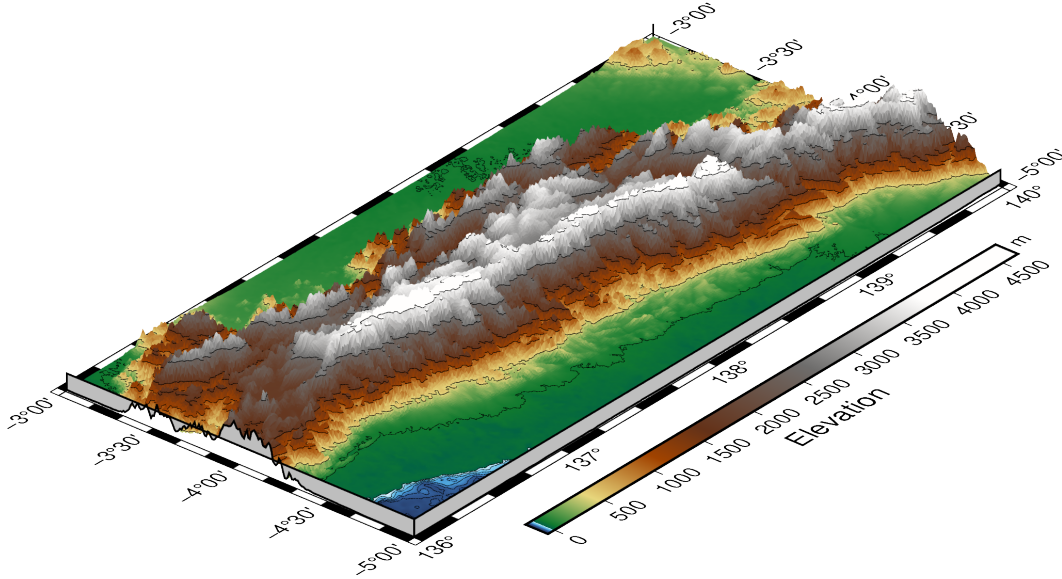


Figure 1: Digital Elevation Model (DEM) of the central highlands of West Papua (rendered using PyGMT (13)).

42 2 Long-term drought / pluvial time-series reconstruction

43 In this part, we reconstruct long-term meteorological drought/pluvial events over the central high-
 44 lands of West Papua. We use SPI-12 (14; 15) as the standard for measuring long-term meteorological
 45 drought/pluvial events that successfully used to reconstruct drought throughout the past millennium
 46 period over the IMC (16).

47 The first step we take, is to calculate the spatial average of land precipitation over the central high-
 48 lands of West Papua using the ERA5 monthly averaged data on single levels (12). Spatial average
 49 of a precipitation field $\bar{p}(\phi, \theta, t)$ on a sphere (17) is mathematically defined in the equation (1),

$$\bar{p}(t) = \frac{1}{4\pi} \int \int p(\phi, \theta, t) \cos(\phi) d\phi d\theta \quad (1)$$

50 , where ϕ is latitude, θ is longitude, and t is time. To handle the gridded dataset, a discretized form
 51 of equation (1) is needed. The discrete form of equation (1) for a grid resolution $\Delta\phi \times \Delta\theta$ is defined
 52 in equation (2),

$$\bar{p}(t) = \sum_{i,j} p(i, j, t) \frac{\cos(\phi_{i,j}) \Delta\phi \Delta\theta}{4\pi} \quad (2)$$

53 , where (i, j) are coordinate indices for each the grid box of precipitation data over the central
 54 highlands of West Papua, and ϕ and θ are in radian. Since ERA5 precipitation data has a spatial res-
 55 olution of $0.25^\circ \times 0.25^\circ$, then $\Delta\phi = \Delta\theta = (0.25/180)\pi = \pi/720$. By substituting this information
 56 into equation (2), the following equation is obtained,

$$\bar{p}(t) = \sum_{i,j} p(i, j, t) \frac{\cos(\phi_{i,j}) (1/720)^2}{4} \quad (3)$$

57 We solve the calculation in the equation (3) using the built-in function in the **xarray** library (18) in
 58 the Python computational environment.

59 The calculation result of equation (3) is the spatial average of monthly precipitation time-series
 60 shown in Figure 2. Figure 2 shows that rainfall events occurred in each month in this period of
 61 study. To see the pattern of monthly rainfall, we average the data for each month, as shown in Figure
 62 3. It can be seen in Figure 3 that the monthly rainfall pattern in the central highlands of West Papua
 63 has one peak and one trough, which corresponds to the rainfall pattern in Region A (19) with a shift
 64 in the onset of wet and dry seasons which is thought to be caused by other local factors. The seasonal
 65 rainfall patterns over the central highlands of West Papua (Figure 3) seem to follow an asymmetric
 66 pattern between boreal summer and winter and between boreal spring and fall.

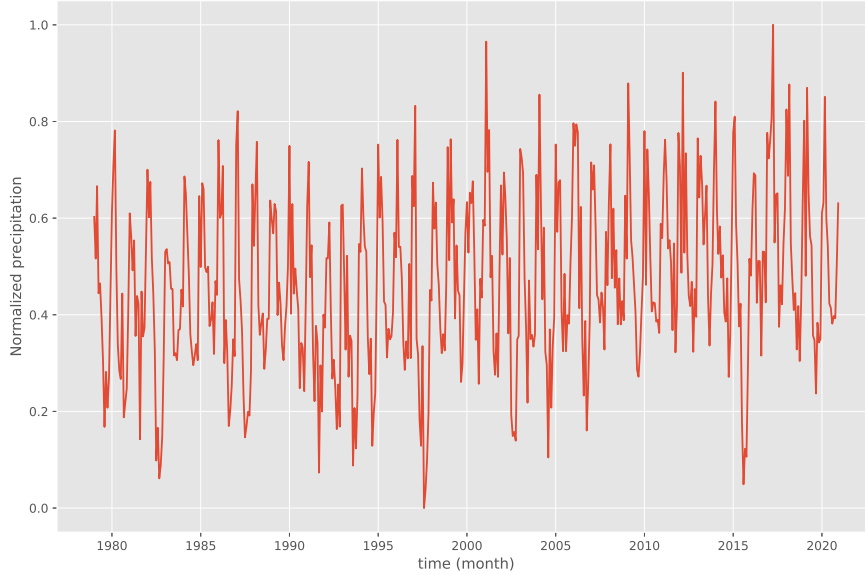


Figure 2: Variations in the normalized monthly precipitation data from ERA5 over the central highlands of West Papua from January 1979 to December 2020.

67 The spatial average of monthly precipitation is then used as input for the calculation of SPI-12.
 68 SPI-12 itself is the comparison of rainfall for 12 consecutive months with the same 12 consecutive
 69 months from previous years. The SPI on this time scale reflects long-term rainfall patterns (14;
 70 15).The time scale is the cumulative of previous periods that may be above or below normal. SPI
 71 on this scale can be related to streamflows, reservoir conditions, and even groundwater content. In
 72 several countries the SPI-12 is most closely related to the Palmer Drought Severity Index (PDSI)
 73 and it is also possible that both indices reflect the same conditions (20).

74 SPI is calculated using statistical methods as follows,

$$G(x) = \int_0^x g(x, \hat{\alpha}, \hat{\beta}) dx = \frac{1}{\hat{\beta} \hat{\alpha} \Gamma(\hat{\alpha})} \int_0^x x^{\hat{\alpha}-1} e^{-x/\hat{\beta}} dx \quad (4)$$

75 , where α is a shape parameter, β is a scale parameter, $\Gamma(\alpha)$ is a gamma function, and x is precipi-
 76 tation values. Equation (4) applies if $x > 0$ (otherwise $g(x, \hat{\alpha}, \hat{\beta}) = 0$, which in this case applies to
 77 precipitation data which are always within the range $(0, +\infty)$). In order to match the gamma distri-
 78 bution with precipitation data, it is necessary to estimate the α and β parameters using the maximum
 79 likelihood approximation which is defined as follows,

$$\hat{\alpha} = \frac{1}{4A} \left(1 + \sqrt{\frac{4A}{3}} \right) \quad (5)$$

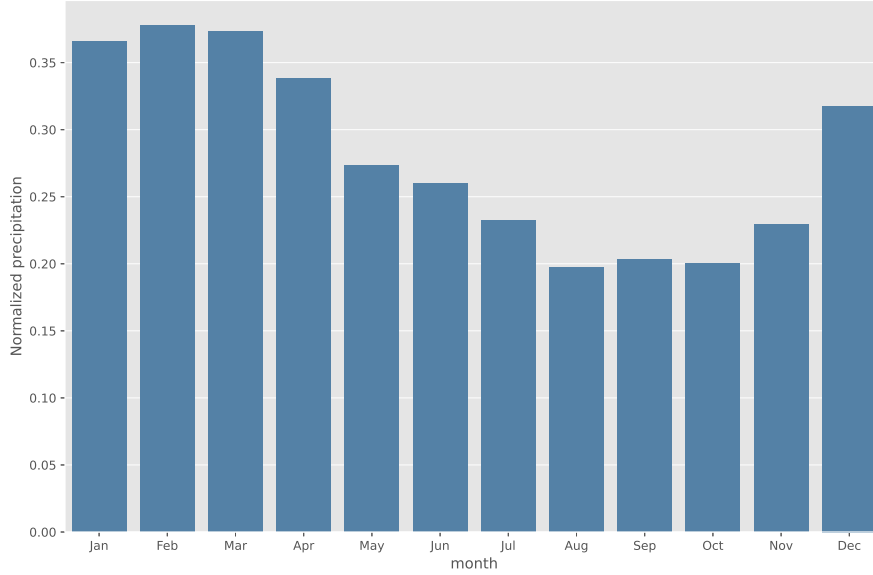


Figure 3: Normalized average monthly precipitation over the central highlands of Papua.

80

$$\hat{\beta} = \frac{\bar{x}}{\hat{\alpha}} \quad (6)$$

81 , where A is defined by equation (7),

$$A = \ln(\bar{x}) - \frac{\sum \ln(x)}{n} \quad (7)$$

82 , where n is the number of observations. For $\hat{\alpha} > 0$, $\Gamma(\hat{\alpha})$ is defined by equation (8),

$$\Gamma(\hat{\alpha}) = \int_0^{+\infty} x^{(\hat{\alpha}-1)} e^{-x} dx \quad (8)$$

83 The gamma distribution is undefined for $x = 0$ and $q = P(x = 0) > 0$, where q is the probability
84 of zero percipitation. Therefore the cumulative probability distribution is defined by equation (9),

$$H(x) = q + (1 - q)G(x) \quad (9)$$

85 The gamma distribution $G(x)$ is then converted to be a normal standard with zero mean and standard
86 deviation of one, so that the SPI index Z is obtained using equation (10),

$$Z = \begin{cases} -t - \frac{c_0 + c_1 t + c_2 t^2}{1 + d_1 t + d_2 t^2 + d_3 t^3}, & \text{for } 0 < H(x) \leq 0.5 \\ t - \frac{c_0 + c_1 t + c_2 t^2}{1 + d_1 t + d_2 t^2 + d_3 t^3}, & \text{for } 0.5 < H(x) < 1 \end{cases} \quad (10)$$

87 , where t is defined by equation (11),

$$t = \begin{cases} \sqrt{\ln\left(\frac{1}{(H(x))^2}\right)}, & \text{for } 0 < H(x) \leq 0.5 \\ \sqrt{\ln\left(\frac{1}{(1-H(x))^2}\right)}, & \text{for } 0.5 < H(x) < 1 \end{cases} \quad (11)$$

88 , and the constants are defined as follows,

$$c_0 = 2.515517, c_1 = 0.802853, c_2 = 0.010328, d_1 = 1.432788, d_2 = 0.109269, d_3 = 0.001308 \quad (12)$$

89 In order to simplify the calculation process, we use the **SPEI** package (21) in the R computational
 90 environment. The result of the SPI-12 reconstruction for the period January 1980 to December 2020
 91 is shown in Figure 4.

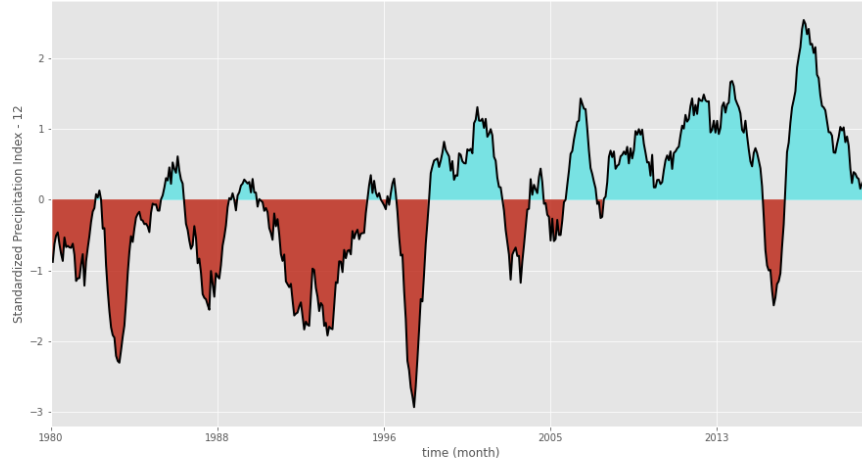


Figure 4: SPI values over the central highlands of West Papua from January 1980 to December 2020 with a 12-month time scale. Negative SPI-12 describes dry conditions (red), whereas positive SPI-12 describes wet conditions (blue).

92 3 Identifying ENSO-driven pattern in SPI-12

93 The influence of the ENSO signal in the IMC (7; 10; 22) is a fact that should not be ignored in the
 94 analysis of drought/pluvial events in the central highlands of West Papua. In this section we discuss
 95 the temporal effect of ENSO, using Multivariate ENSO Index (MEI) (23), on SPI-12. To measure
 96 the temporal effect of ENSO on drought/pluvial events over the area of study, we use the popular
 97 algorithm for measuring geophysical signal patterns, i.e. wavelet transforms. The advantage of
 98 wavelet transforms compared to other power spectrum methods is that they can capture non-linear
 99 signals from time series because they use small wave packets (wavelets) as the base functions which
 100 intrinsically have smooth ends, instead of using sine and cosine wave functions (24).

101 In this study we use an extension of the Morlet wavelet (ψ) (25) to model ENSO and SPI-12 signals,
 102 which is defined by,

$$\psi(t) = \pi^{-\frac{1}{4}} e^{-i\omega_0 t} e^{-\frac{1}{2}t^2}, t = 1, 2, 3, \dots \quad (13)$$

103 , where t is the position where the wavelet operates in a time series with a narrow range of observa-
 104 tions.

105 In general, wavelets have two main components, namely time or position k and frequency f . The k
 106 parameter has an important role in detecting the exact location of a wavelet by relocating the wavelet
 107 over a period of time, while f is useful for monitoring the convex wavelet to localize different
 108 frequencies. By transforming ψ , we get the $\psi_{k,f}$ parameter as follows,

$$\psi_{k,f}(t) = \frac{1}{\sqrt{h}} \psi\left(\frac{t-k}{f}\right), k, f \in \mathbb{R}, f \neq 0 \quad (14)$$

109 Equation (15) describes the modeling of a time series $x(t)$ into a wavelet transform,

$$W_x(k, f) = \int_{-\infty}^{+\infty} x(t) \frac{1}{\sqrt{f}} \psi\left(\frac{(t-k)}{f}\right) dt \quad (15)$$

110 The signal power in the time series $x(t)$ itself is measured using the wavelet power spectrum
 111 $WPS_x(k, f)$ which is defined as follows,

$$WPS_x(k, f) = |W_x(k, f)|^2 \quad (16)$$

112 In order to simplify the process of calculating the continuous wavelet power spectrum on ENSO and
 113 SPI-12 data, we use the **PyCWT** library (26) in the Python computational environment.

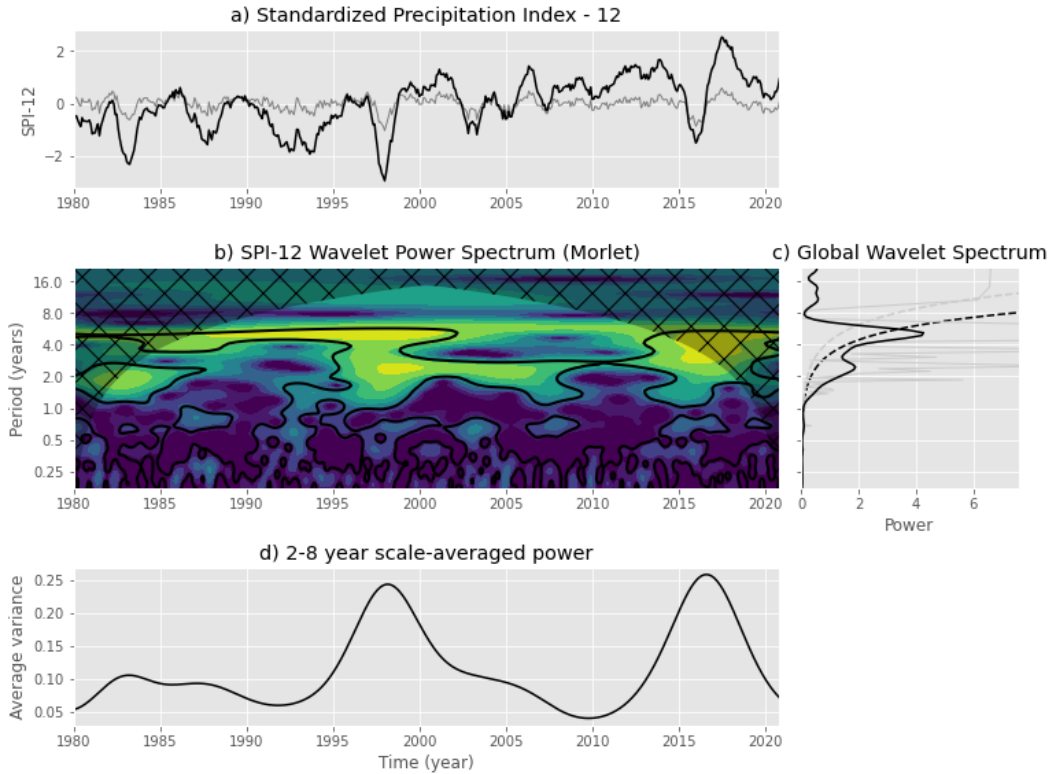


Figure 5: Continuous wavelet transform for the SPI-12. These plots clearly shows significant periodicity at 2 - 8 year cycle.

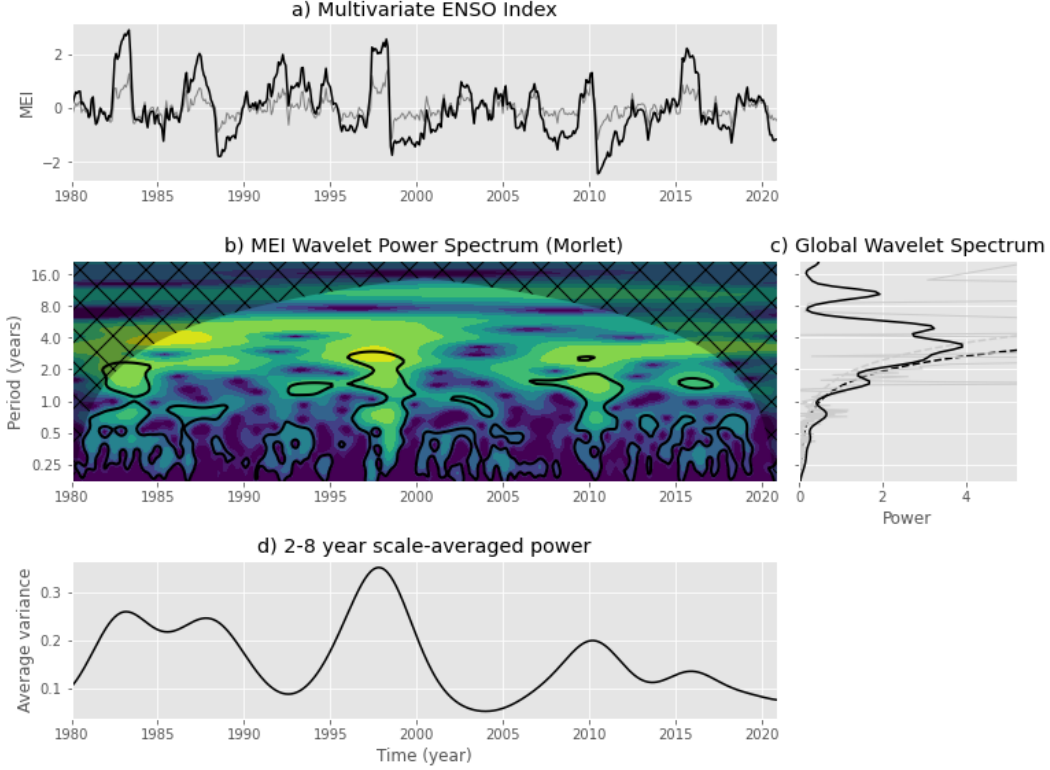


Figure 6: Continuous wavelet transform for the MEI. These plots clearly shows significant periodicity at 2 - 8 year cycle.

114 There are similarities of WPS between ENSO (Figure 6) and SPI-12 (Figure 5). However, to mea-
 115 sure the relationship between the two quantitatively, I need another mathematical tool, namely the
 116 wavelet coherence (WTC). We use WTC to find time-frequency-based causality between two time-
 117 series data, in this context MEI. $x(t)$ and SPI-12 $y(t)$. The first step we take is to find the cross
 118 wavelet transform (XWT) of the two time-series data (equation (17)),

$$W_{xy}(k, f) = W_x(k, f)\overline{W_y(k, f)} \quad (17)$$

119 , where $W_{x,y}(k, f)$ is the XWT of the two time-series data. Then to find WTC value, the equation
 120 (18) is used as follows,

$$R^2(k, f) = \frac{|C(f^{-1}W_{xy}(k, f))|^2}{C(f^{-1}|W_x(k, f)|^2)C(f^{-1}|W_y(k, f)|^2)} \quad (18)$$

121 , C parameter shows the time and smoothing process over the duration of time in within the range
 122 of $0 \leq R^2(k, f) \leq 1$. When $R^2(k, f)$ approaches one, a strong correlation can be expected be-
 123 tween MEI and SPI-12 (indicated by light yellow color surrounded by a black line in the figure 7).
 124 Conversely, if $R^2(k, f)$ is zero, then there is no correlation between the two variables. To find out
 125 the positive or negative correlation of the two time-series data, we use the phase difference equation
 126 (equation (19)) as follows,

$$\phi_{xy}(k, f) = \arctan \left(\frac{\Im \left\{ C(f^{-1}W_{xy}(k, f)) \right\}}{\Re \left\{ C(f^{-1}W_{xy}(k, f)) \right\}} \right) \quad (19)$$

127 , where \Re shows the real part and \Im shows the imaginary part. To simplify the WTC calculation
 128 process, we use the open source MATLAB[®] Toolbox by (author?) (27).

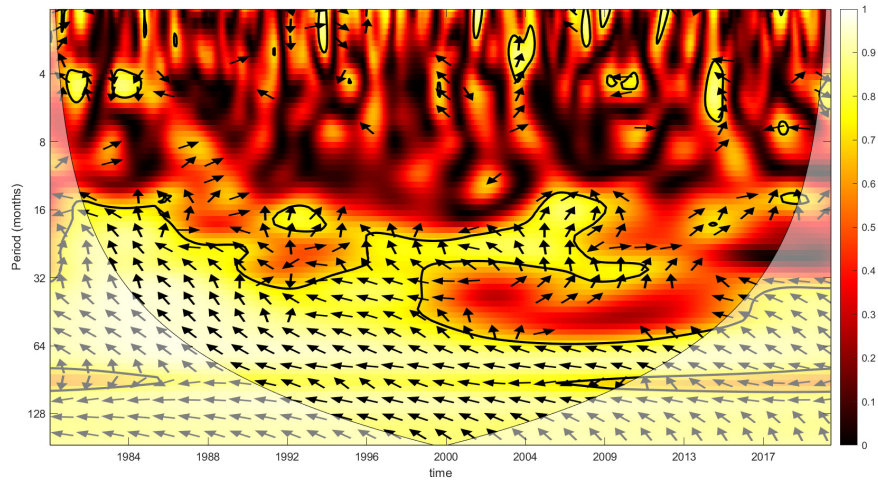


Figure 7: Wavelet coherence between MEI and SPI-12. The color scale on the right side of the figure represents the level of correlation between ENSO and long-term meteorological drought/pluvial events over the central highlands of West Papua. The light yellow color indicates high correlations among the variables, while the thick black contour designates the 5% significance level against red noise and the cone of influence (COI) where edge effects might distort the picture is shown as a lighter shade. The arrows show the phasing direction (**right**: in-phase, **left**: anti-phase, **down**: MEI leading SPI-12 by $\pi/2$, **up**: SPI-12 leading MEI by $\pi/2$).

129 As seen in Figure 7, WTC can capture the negative relationship between MEI and SPI-12 at 32 to
 130 128 month periodicity. This causal effect reveals that precipitation over the central highlands of
 131 West Papua increases during La Niña and decreases during El Niño.

132 **4 ENSO - SPI-12 dynamic relationship and predictability**

133 In order to produce accurate SPI-12 predictions, we use Nonlinear Autoregressive with Exogenous
 134 input neural networks (NARX) model to capture the dynamic relationship between ENSO and long-
 135 term drought/pluvial events over the central highlands of West Papua. NARX is a type of recurrent
 136 dynamic neural networks that is widely used to model nonlinear relationships from attributes in a
 137 time series (28; 29; 30). A simple NARX diagram can be seen in Figure 8. Inputs are entered into
 138 delay units, which act as memory for the previous inputs. The outputs from NARX are also stored
 139 in delay units, which are then entered directly into hidden units.

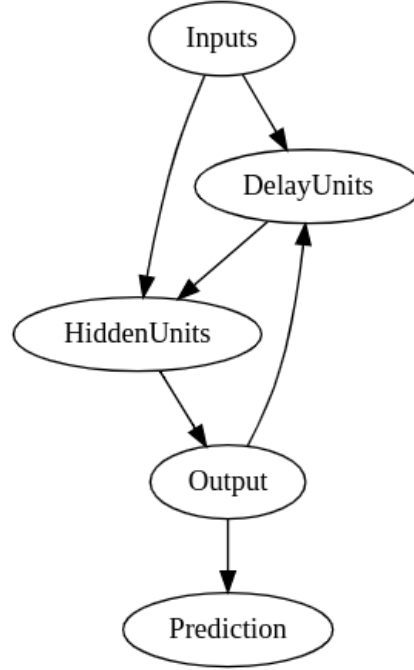


Figure 8: Simple schematic diagram of NARX model.

140 NARX model is defined as a nonlinear mapping function f (28) as follows,

$$y_t = f(y_{t-1}, y_{t-2}, \dots, y_{t-d_y}, x_{t-1}, x_{t-2}, \dots, x_{t-d_x}) \quad (20)$$

141 , where y is a target (SPI-12) and x are attributes (MEI); and $d_x \geq 1$, $d_y \geq 1$, $d_y \geq d_x$ are
 142 delays. The nonlinear f function itself is generally unknown, and must be approximated using the
 143 existing data. There are various ways to approximate this function, in this study we use multilayer
 144 perceptrons provided by **PyNeurGen** library (31) in the Python computational environment. We
 145 use 1 time steps of delay for each of the input (x) and output (y) attributes. In addition, we also
 146 split incoming weights, 60% for MEI and 30% for SPI-12. We make use of the following sigmoid
 147 function for activation of the perceptrons,

$$S(x) = \frac{1}{1 + e^{-x}} \quad (21)$$

148 We divided SPI-12 into two parts, 85% for the training set and 15% (January 1980 - December 2014)
 149 for the testing set (January 2015 - December 2020). We use a moderate steps of learning rate of 35%
 150 for the optimization process using the Stochastic Gradient Descent (SGD) algorithm. Our NARX
 151 model is run for 10 epochs without activating the random testing parameter to maintain the order of
 152 time-series data. To evaluate the model performance, we use the Mean Squared Error (MSE) which
 153 is shown by equation (22) below,

$$MSE = \frac{1}{n} \sum_{i=1}^n (\hat{y}_i - y_i)^2 \quad (22)$$

154 , which is the sum series of the squared differences of the observed target y_i and predicted values
 155 \hat{y}_i , which is then divided by the total number of test samples n . The MSE at each training epoch
 156 can be seen in Figure 9. It exhibits sharp decline at the first epoch and finally leveling out until the
 157 end of the last training epoch. The overall MSE evaluation result in the test set is 0.011341. The
 158 comparison between the NARX model prediction results and the actual SPI-12 is shown in Figure
 159 10. Overall, the model tends to overestimate and underestimate certain extreme values, although it
 160 adequately captures the general pattern of SPI-12.

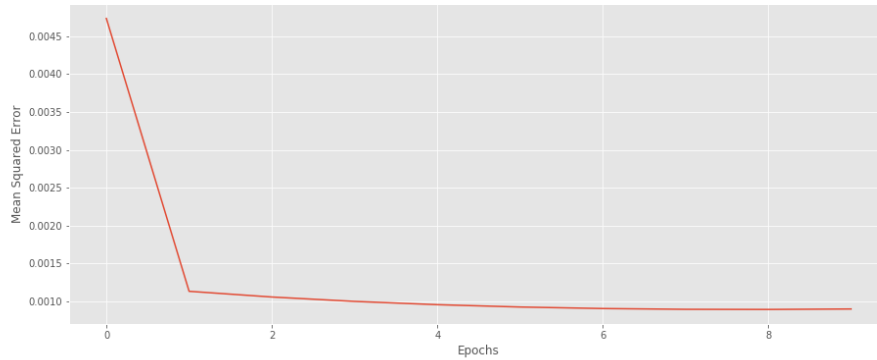


Figure 9: MSE by epoch for NARX model.

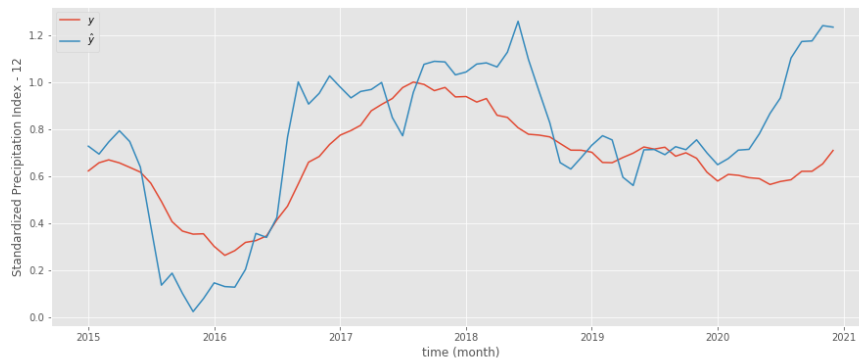


Figure 10: Actual y (red) and predicted \hat{y} (blue) SPI-12 values for NARX model.

161 5 Concluding remarks and future work suggestions

162 We have performed time series analysis of the SPI-12 over the central highlands of West Papua. We
 163 found time series teleconnection pattern between ENSO and hydrometeorological drought / pluvial
 164 events in this region through wavelet transformations. Our result suggests that ENSO is negatively
 165 correlated to the long-term rainfall pattern in this region. We use the patterns obtained from the
 166 WTC to model the temporal dynamics between ENSO - long-term rainfall patterns using the NARX
 167 algorithm. The prediction results from the NARX model can capture the general pattern of the
 168 underlying dynamics of SPI-12.

169 The study suggests possible extension of the work by using different fine-tuned optimization
 170 schemes on the NARX model (32) and using early-stopping algorithms (33) to avoid training over-
 171 fitting. In addition, a comparison of more powerful seq2seq machine learning algorithms such as
 172 Long-Short Term Memory (LSTM) (34), Gated Recurrent Unit (GRU) (35), and DeepAR (36) is
 173 also needed to select the time-series model that best represents the data. Comparison and data as-
 174 similation with Global Climate Model (GCM) outputs is also needed to understand the physical
 175 process of the spatio-temporal dynamics between ENSO and long-term rainfall patterns over the
 176 central highlands of West Papua.

177 Acknowledgements

178 The author is indebted many thanks to Cristy Q. Ho, Faiz R. Fajary, Muhammad R. Syahputra,
 179 Nurjanna J. Trilaksono, and Michael N. Evans for fruitful discussion and critics in preparing the

180 article. The author also thanks Dasapta E. Irawan for sharing the computational resource to run
181 the statistical models. The author gratefully thank Herho Group Corp., Rialto, CA for the financial
182 support. The code and datasets used for this work are posted on GitHub at <https://github.com/sandyherho/tsHydrochWP>.
183

184 References

- 185 [1] C. J. Pigram and P. A. Symonds, “A review of the timing of the major tectonic events in the
186 new guinea orogen,” *Journal of Southeast Asian Earth Sciences*, vol. 6, no. 3, pp. 307–318,
187 1991.
- 188 [2] T. R. Charlton, “Tertiary evolution of the eastern indonesia collision complex,” *Journal of*
189 *Asian Earth Sciences*, vol. 18, no. 5, pp. 603–631, 2000.
- 190 [3] D. B. Dow and R. Sukamto, “Western irian jaya: The end-product of oblique plate convergence
191 in the late tertiary,” *Tectonophysics*, vol. 106, no. 1, pp. 109–139, 1984.
- 192 [4] C. S. Ramage, “Role of a tropical “maritime continent” in the atmospheric circulation,”
193 *Monthly Weather Review*, vol. 96, no. 6, pp. 365 – 370, 1968.
- 194 [5] C.-P. Chang, Z. Wang, J. McBride, and C.-H. Liu, “Annual cycle of southeast asia—maritime
195 continent rainfall and the asymmetric monsoon transition,” *Journal of Climate*, vol. 18, no. 2,
196 pp. 287 – 301, 2005.
- 197 [6] J. Boerema, *Van Den Typen Regenval in Nederlandsch Indie (Rainfall types in Nederlands*
198 *Indies)*. The Royal Observatory Magnetisch En Meteorologisch Batavia, Batavia, 1938.
- 199 [7] D. S. Permana, L. G. Thompson, and G. Setyadi, “Tropical west pacific moisture dynamics
200 and climate controls on rainfall isotopic ratios in southern papua, indonesia,” *Journal of Geo-*
201 *physical Research: Atmospheres*, vol. 121, no. 5, pp. 2222–2245, 2016.
- 202 [8] A. Marshall and B. M. Beehler, *The Ecology of Papua*, vol. 1. Singapore: Periplus Editions
203 (HK), 2007.
- 204 [9] B. Goger, M. W. Rotach, A. Gohm, I. Stiperski, and O. Fuhrer, “Current challenges for nu-
205 merical weather prediction in complex terrain: Topography representation and parameteriza-
206 tions,” in *2016 International Conference on High Performance Computing Simulation (HPCS)*,
207 pp. 890–894, 2016.
- 208 [10] M. D. Yamanaka, “Physical climatology of indonesian maritime continent: An outline to com-
209 prehend observational studies,” *Atmospheric Research*, vol. 178-179, pp. 231–259, 2016.
- 210 [11] C. D. Peters-Lidard, M. Clark, L. Samaniego, N. E. C. Verhoest, T. van Emmerik, R. Uijlen-
211 hoet, K. Acheng, T. E. Franz, and R. Woods, “Scaling, similarity, and the fourth paradigm for
212 hydrology,” *Hydrology and Earth System Sciences*, vol. 21, no. 7, pp. 3701–3713, 2017.
- 213 [12] H. Hersbach, B. Bell, P. Berrisford, S. Hirahara, A. Horányi, J. Muñoz-Sabater, J. Nicolas,
214 C. Peubey, R. Radu, D. Schepers, A. Simmons, C. Soci, S. Abdalla, X. Abellan, G. Balsamo,
215 P. Bechtold, G. Biavati, J. Bidlot, M. Bonavita, G. De Chiara, P. Dahlgren, D. Dee, M. Dia-
216 mantakis, R. Dragani, J. Flemming, R. Forbes, M. Fuentes, A. Geer, L. Haimberger, S. Healy,
217 R. Hogan, E. Hólm, M. Janisková, S. Keeley, P. Laloyaux, P. Lopez, C. Lupu, G. Radnoti,
218 P. de Rosnay, I. Rozum, F. Vamborg, S. Villaume, and J. Thépaut, “The era5 global reanaly-
219 sis,” *Quarterly Journal of the Royal Meteorological Society*, vol. 146, no. 730, pp. 1999–2049,
220 2020.
- 221 [13] P. Wessel, J. F. Luis, L. Uieda, R. Scharroo, F. Wobbe, W. H. F. Smith, and D. Tian, “The
222 generic mapping tools version 6,” *Geochemistry, Geophysics, Geosystems*, vol. 20, no. 11,
223 pp. 5556–5564, 2019.
- 224 [14] T. B. McKee, N. J. Doesken, and J. Kleist, “The relationship of drought frequency and duration
225 of the time scales,” in *Proceeding 8th Conference on Applied Climatology*, (Anaheim, CA),
226 American Meteorological Society, 1993.

- 227 [15] N. B. Guttman, “Accepting the standardized precipitation index: A calculation algorithm1,”
228 *Journal of the American Water Resources Association*, vol. 35, no. 2, pp. 311–322, 1999.
- 229 [16] S. Herho, M. R. Syahputra, and R. Suwarman, “A preliminary study of meteorological drought
230 influences to social events over the maritime continent during the last millennium,” in *Extended*
231 *Abstract 98th American Meteorological Society Annual Meeting*, 16th History Symposium,
232 (Austin, TX), American Meteorological Society, 2018.
- 233 [17] S. S. P. Shen and R. C. J. Somerville, *Climate Mathematics: Theory and Applications*. Cam-
234 bridge University Press, 2019.
- 235 [18] S. Hoyer and J. Hamman, “xarray: N-D labeled arrays and datasets in Python,” *Journal of*
236 *Open Research Software*, vol. 5, no. 1, 2017.
- 237 [19] E. Aldrian and R. D. Susanto, “Identification of three dominant rainfall regions within indone-
238 sia and their relationship to sea surface temperature,” *International Journal of Climatology*,
239 vol. 23, no. 12, pp. 1435–1452, 2003.
- 240 [20] G. M. Guenang and F. M. Kamga, “Computation of the standardized precipitation index (spi)
241 and its use to assess drought occurrences in cameroon over recent decades,” *Journal of Applied*
242 *Meteorology and Climatology*, vol. 53, no. 10, pp. 2310 – 2324, 2014.
- 243 [21] S. Beguería and S. Vicente-Serrano, *SPEI: Calculation of the Standardised Precipitation-*
244 *Evapotranspiration Index*, 2017. R package version 1.7.
- 245 [22] S. Yoden, S. Otsuka, N. J. Trilaksono, and T. W. Hadi, *Recent Progress in Research on the*
246 *Maritime Continent Monsoon*, ch. Chapter 6, pp. 63–77. 2017.
- 247 [23] K. Wolter and M. S. Timlin, “El niño/southern oscillation behaviour since 1871 as diagnosed in
248 an extended multivariate enso index (mei.ext),” *International Journal of Climatology*, vol. 31,
249 no. 7, pp. 1074–1087, 2011.
- 250 [24] K.-M. Lau and H. Weng, “Climate signal detection using wavelet transform: How to make a
251 time series sing,” *Bulletin of the American Meteorological Society*, vol. 76, no. 12, pp. 2391 –
252 2402, 1995.
- 253 [25] C. Torrence and G. P. Compo, “A practical guide to wavelet analysis,” *Bulletin of the American*
254 *Meteorological Society*, vol. 79, no. 1, pp. 61 – 78, 1998.
- 255 [26] S. Krieger, N. Freijj, A. Brazhe, C. Torrence, and G. P. Compo, *PyCWT: spectral analysis using*
256 *wavelets in Python*, 2017. Python library version 0.3.0a22.
- 257 [27] A. Grinsted, J. C. Moore, and S. Jevrejeva, “Application of the cross wavelet transform and
258 wavelet coherence to geophysical time series,” *Nonlinear Processes in Geophysics*, vol. 11,
259 no. 5/6, pp. 561–566, 2004.
- 260 [28] E. Diaconescu, “The use of narx neural networks to predict chaotic time series,” *World Scien-*
261 *tific and Engineering Academy and Society (WSEAS)*, vol. 3, no. 3, p. 182–191, 2008.
- 262 [29] M. R. C. O. Ang, R. M. Gonzalez, and P. P. M. Castro, “Multiple data fusion for rainfall
263 estimation using a NARX-based recurrent neural network – the development of the REIINN
264 model,” *IOP Conference Series: Earth and Environmental Science*, vol. 17, p. 012019, 2014.
- 265 [30] J. M. Caswell, “A nonlinear autoregressive approach to statistical prediction of disturbance
266 storm time geomagnetic fluctuations using solar data,” *Journal of Signal and Information Pro-*
267 *cessing*, vol. 5, pp. 42–53, 2014.
- 268 [31] D. Smiley, *PyNeurGen: Python Neural Genetic Algorithm Hybrids*, 2012. Python library
269 version 0.3.1.
- 270 [32] X. He, K. Zhao, and X. Chu, “Automl: A survey of the state-of-the-art,” *Knowledge-Based*
271 *Systems*, vol. 212, p. 106622, 2021.

- 272 [33] R. Gençay and M. Qi, “Pricing and hedging derivative securities with neural networks:
273 Bayesian regularization, early stopping, and bagging,” *IEEE Transactions on Neural Networks*,
274 vol. 12, pp. 726 – 734, 08 2001.
- 275 [34] S. Hochreiter and J. Schmidhuber, “Long Short-Term Memory,” *Neural Computation*, vol. 9,
276 no. 8, pp. 1735–1780, 1997.
- 277 [35] F. A. Gers, J. Schmidhuber, and F. Cummins, “Learning to forget: continual prediction with
278 lstm,” in *1999 Ninth International Conference on Artificial Neural Networks ICANN 99. (Conf.*
279 *Publ. No. 470)*, vol. 2, pp. 850–855, 1999.
- 280 [36] D. Salinas, V. Flunkert, J. Gasthaus, and T. Januschowski, “Deepar: Probabilistic forecasting
281 with autoregressive recurrent networks,” *International Journal of Forecasting*, vol. 36, no. 3,
282 pp. 1181–1191, 2020.